Electromagnetic flow control in the Ribbon Growth on Substrate (RGS) process

Beckstein, P.; Galindo, V.; Gerbeth, G.;

Originally published:

August 2015

Magnetohydrodynamics 51(2015)2, 385-396

Perma-Link to Publication Repository of HZDR:

https://www.hzdr.de/publications/Publ-20320

ELECTROMAGNETIC FLOW CONTROL IN THE RIBBON GROWTH ON SUBSTRATE PROCESS

P. Beckstein, V. Galindo, G. Gerbeth

Helmholtz-Zentrum Dresden – Rossendorf (HZDR),
Bautzner Landstrasse 400, 01328 Dresden, Germany

The Ribbon Growth on Substrate (RGS) technology promises a very efficient approach for future photovoltaic (PV) silicon wafer production compared to the majority of commonly accepted processes. Although, for an eventual break-through of this RGS technology a number of remaining problems need to be addressed to increase the process stability. We have, therefore, performed numerical investigations in order to study the influence of the involved AC magnetic fields on the silicon melt flow during the RGS process.

Introduction. Today photovoltaic silicon is mainly produced by directional solidification of multi-crystalline silicon or by the Czochralski method of silicon single crystal growth. Wafers are then produced by sawing the ingots. The unavoidable sawing losses of prevalent processes are still in the range of 40 to 50% of the fed material. A very efficient way to avoid this deficit in terms of energy and material is the Ribbon Growth on Substrate (RGS) technology, which was suggested and developed during the last decades [1–5].

The basic idea of this process is a continuous feeding of molten silicon into a casting frame without bottom, whereas a solidified silicon foil is extracted sidewise on a sub-cooled moving substrate underneath. This brings both a close to perfect material yield by avoiding sawing losses and a low energy consumption due to the continuous nature of the processing. Nearly all of the silicon melt is directly used to form the wafer itself. Another distinct advantage of the RGS process also comes from its fully decoupled solidification and casting velocities. Fig. 1 shows a schematic of this principle. The blueprint depicts one half of the core process assembly, where the foreground corresponds to a central sectional plane in the process direction. The narrow region between the bottom of the casting frame walls and the substrate has the shape of a spacious slit.

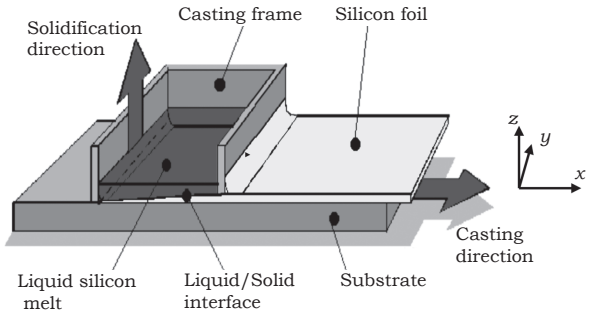

Fig. 1. Scheme of the RGS process without excitation coils [2]: one half with central cut in the process direction. The narrow slit region is situated between the casting frame and the substrate.

Table 1. Properties for different materials: density ρ, kinematic viscosity η, electrical conductivity σ, surface tension γ and skin depth $\delta = \sqrt{1/(\pi f \mu_0 \sigma)}$ assuming a frequency of $f = 10\,\mathrm{kHz}$.

Material	ρ [kg/m^3]	η [Pa·s]	σ [S/m]	γ [N/m]	δ [mm]
Liquid silicon	2580	0.86×10^{-3}	1.20×10^{6}	0.733	5.0
Solid silicon	2330	-	8.30×10^{4}	-	17.0
Graphite	1880	-	1.25×10^{5}	-	14.0
Copper	8960	-	6.00×10^{7}	-	0.7

A challenging task in realizing this idea technically is the need to fully control the liquid silicon outflow. The AC magnetic fields, which are used for melting inductively the silicon, bear a two-fold meaning. That is, a single excitation coil provides both an inductive heater of the casting frame and a kind of magnetic valve. The latter actively prevents leakage in the slit regions and reduces oscillations at the extraction site of the silicon foil through electromagnetic forces. This Lorentz force field acts to counter the gravitational forces on the melt, but the valve works only because of additional capillarity effects based on strong surface tension. As this effect can be influenced to take advantage, there is a considerable interest in gaining a better understanding of the magnetohydrodynamics of the RGS process. Recent activities on electromagnetic retention for liquid silicon have been reported in [6].

A major problem of the RGS process which still has to be addressed is the occurrence of flow instabilities and meniscus oscillations at the open slit, where the moving substrate enters and leaves the casting frame. There is only very limited literature about numerical simulations of the silicon melt flow for the RGS process (e.g., [7, 8]). Moreover, all related simulations were mainly focused on the crystallization process and solidification front shape of silicon ribbons. In contrast, we have performed numerical investigations in order to study the influence of the involved AC magnetic fields on the silicon melt during the RGS process.

1. Modelling overview. A typical associated process parameter set, which evolved mainly from empirical analysis, is an RMS-current of $I_{\mathrm{RMS}} = 1000\,\mathrm{A}$ at a frequency of $f = 10\,\mathrm{kHz}$ to feed the excitation coils, in combination with a substrate velocity $u_S = 0.1\,\mathrm{m/s}$. The most important properties of the involved materials, as shown in Fig. 1, are listed in Table 1.

The casting region in the real RGS prototype machine [2] is a very complex and detailed system. Especially the difference in scale between, e.g., the casting frame of width of 156 mm in relation to the magnetic valve at the wafer exit side of less than 1 mm is challenging for grid definition and computing capacity. Therefore, a simplified set of modelling parameters and casting environment geometry was developed. It is expected that this simplified model allows the calculation of the main effects of the liquid silicon behavior, and its results should allow a comparison to real process data from the RGS process. In this simplified model, the RGS wafer size is given by 156 mm × 156 mm × 0.4 mm. A typical melt level height inside the casting frame varies between $h = 10\,\mathrm{mm}$ and $h = 30\,\mathrm{mm}$. In Fig. 2, one can find detailed drawings of the model side (left) and top (right) view. All remaining dimensions can also be found there.

To study the interplay of magnetic fields and fluid dynamics in the case of the RGS process, a comprehensive model has to correctly represent a fully three-dimensional and two-way-coupled system of AC magnetic fields and fluid flow with

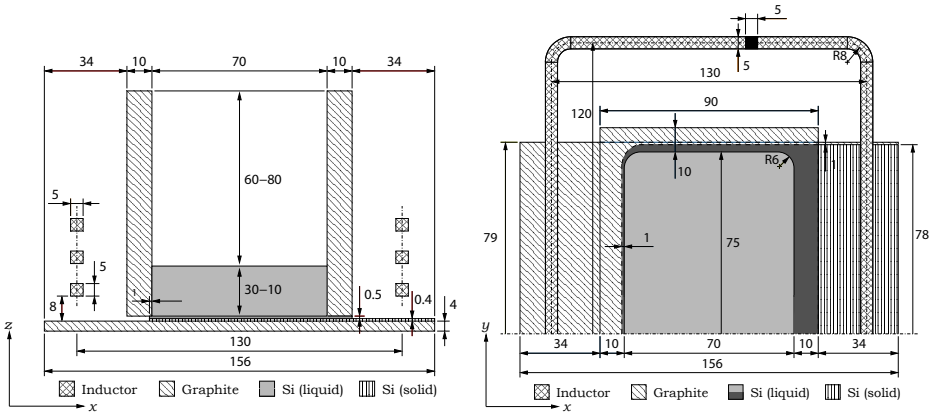

Fig. 2. Simplified numerical model geometry (dimensions in mm). The drawing on the left represents both a central longitudinal section of the actual 3D-model and a derived 2D-version. On the right: the top view of one model half is displayed.

free surfaces at the slit and at top of the melt in the crucible. Furthermore, the model has to account for the material values given above. The latter particularly means dealing correctly with electrical conductivities of different orders of magnitude and very high surface tension forces at the interface between the silicon melt and its surrounding atmosphere.

The magnetic fields may be described using the $\mathbf{A}$-V-formulation of the quasi-static Maxwell equations implying MHD approximations [9]. It can be shown that assuming only a very small magnetic Reynolds number and neglecting magnetization effects is valid for modelling the RGS process with sufficient quality. Thus, the magnetic fields can be described as follows:

$$\mathbf{B} = \nabla \times \mathbf{A}\,; \quad \mathbf{E} = -\left(\partial_t \mathbf{A} + \nabla V\right)\,; \quad \|\mathbf{u} \times \mathbf{B}\| / \|E\| \ll 1\,. \tag{1}$$

Here the magnetic vector potential is denoted by $\mathbf{A}$, the magnetic field by $\mathbf{B}$, the electric field by $\mathbf{E}$, the electric scalar potential by V, the velocity field by $\mathbf{u}$, and the time by t.

Taking the magnetic vector potential with the applied Coulomb gauge $\nabla \cdot \mathbf{A} = 0$ and the electric scalar potential instead of the magnetic and electric field allows us to explicitly introduce an external source current density term $\mathbf{j}_\mathrm{E}(I_\mathrm{RMS})$ into the system, which represents the effect of the excitation coil [9, 10]. In case of a constant ($\nabla\sigma = 0$) or even zero ($\sigma = 0$) electrical conductivity, it can be shown [11] that the scalar potential may be incorporated into the vector potential, if $\mathbf{A}$ is conceptually substituted with a modified version: $\hat{\mathbf{A}} = \mathbf{A} + \int \nabla V \,\mathrm{d}t$. That is, if we imply a constant σ for each material, only $\mathbf{A}$ is required:

$$\nabla \times \nabla \times \mathbf{A} + \sigma\mu_0 \partial_t \mathbf{A} = \mu_0 \mathbf{j}_\mathrm{E}\,; \quad \nabla \cdot \mathbf{A} = 0\,; \tag{2}$$

$$\mathbf{j} = \mathbf{j}_\mathrm{I} + \mathbf{j}_\mathrm{E}\,; \quad \mathbf{j}_\mathrm{I} = -\sigma \partial_t \mathbf{A}\,. \tag{3}$$

The field $\mathbf{j}_\mathrm{I}$ represents the induced current density. To find suitable boundary conditions for the magnetodynamic problem, the numerical domain is divided into several sub-domains. The whole domain is firstly split into three main regions. This comprises a conducting part (melt, graphite and solid silicon), a non-conducting part (assuming there is only a bounded spherical atmosphere surrounding all conducting parts), whose intersection constitutes the outer conductor boundary, and the excitation coil. Secondly, the conducting part is again split into

one sub-region for every simply connected area with a constant electrical conductivity. The second partitioning creates several inner boundaries, where jumps in σ occur. The spherical outer boundary of the non-conducting region is necessary to realize numerically the actual unboundedness. It can be modelled either by using an infinite domain [12] or based on the hypothesis of fully decayed field amplitudes if the size of the sphere is sufficiently large. A detailed mathematical description of all boundary conditions can also be found in [9].

By introducing a complex-valued sinusoidal of the involved harmonic AC fields, Eqs. (2) and (3) may be transformed into their frequency domain for the angular frequency $\omega = 2\pi f$. This approach leads to a quasi-stationary problem since the time derivatives may then be substituted with a complex-valued angular frequency ($\partial/\partial_t = i\omega$).

The momentum balance of the fluid, which is part of the conducting region, depends on the time-averaged Lorentz force,

$$\mathbf{F}_\mathrm{L} = \langle \mathbf{j} \times \mathbf{B} \rangle_t \,. \tag{4}$$

Via the Ampere's law, this force field can be expressed as a sum of its rotational and gradient parts:

$$\mathbf{F}_\mathrm{L} = \mathbf{F}_\mathrm{L,rot} + \mathbf{F}_\mathrm{L,grad}; \tag{5}$$

$$\mathbf{F}_\mathrm{L,rot} = 1/\mu_0 \langle (\mathbf{B} \cdot \nabla)\mathbf{B} \rangle_t \,; \quad \mathbf{F}_\mathrm{L,grad} = -\nabla p_\mathrm{B} \,, \tag{6}$$

where p_B is the time-averaged magnetic pressure given by

$$p_\mathrm{B} = 1/(2\mu_0) \langle \mathbf{B}^2 \rangle_t \,. \tag{7}$$

The fluid dynamics, describing the silicon melt flow, is governed by the principle of conservation of mass and momentum. For our RGS model, this leads to the isothermal, incompressible Navier–Stokes equation [13] with additional terms for gravity and for the time-averaged Lorentz force, as described in Eqs. (4) to (7):

$$\rho \left[\partial_t \mathbf{u} + (\mathbf{u} \cdot \nabla)\, \mathbf{u} \right] = \nabla \cdot \boldsymbol{\tau}' + \mathbf{F}_\mathrm{L,rot}; \quad \nabla \cdot \mathbf{u} = 0; \tag{8}$$

$$\boldsymbol{\tau}' = \eta \left[\nabla \mathbf{u} + (\nabla \mathbf{u})^T \right] - p' \mathbf{I} \,. \tag{9}$$

Here $\boldsymbol{\tau}'$ represents the stress tensor including a modified diagonal fluid pressure,

$$p' = p + p_\mathrm{G} + p_\mathrm{B} \quad \text{with} \quad p_\mathrm{G} = -\rho\, (\mathbf{g} \cdot \mathbf{x}) \,, \tag{10}$$

which includes the fluid pressure p and both the magnetic and the hydrostatic potential (the coordinates $\mathbf{x}$). Surface tension is only acting at free surface boundaries. It is thereby worth to mention that the viscosity of the external atmosphere, which is in contact with the liquid melt at the conductor boundary, is several orders of magnitude smaller than the viscosity of the melt itself. Thus, the fluid boundary condition at the moving free surface with the free surface velocity $\mathbf{u}_\mathrm{I}$, its outward unit normal $\mathbf{n}$, the unit tangent vector $\mathbf{t}$ and a corresponding stress vector $\mathbf{s} = \boldsymbol{\tau}' \cdot \mathbf{n}$ can be modelled using a simplified Young–Laplace equation [14],

$$\mathbf{u} \cdot \mathbf{n} = \mathbf{u}_\mathrm{I} \cdot \mathbf{n}; \tag{11}$$

$$\mathbf{s} \cdot \mathbf{n} = 2\kappa\gamma - (p_\mathrm{E} + p_\mathrm{G} + p_\mathrm{B}) \,; \quad \mathbf{s} \cdot \mathbf{t} = 0; \tag{12}$$

$$\kappa = -1/2\, (\nabla_\Gamma \cdot \mathbf{n}) \,; \quad \nabla_\Gamma = \nabla - \mathbf{n}\partial_\mathbf{n} = \left(\mathbf{I} - \mathbf{n}\mathbf{n}^T \right) \nabla \,. \tag{13}$$

Therein the external fluid appears only through its pressure p_E. The surface gradient operator ∇_Γ defines the mean curvature κ of the free surface and the

surface tension coefficient γ is assumed to be constant (no Marangoni effect). For a fixed ($\mathbf{u}_\mathrm{I} = 0$) and planar surface ($\kappa = 0$), Eqs. (11) and (12) can be simplified again to get a free-slip boundary condition with a fixed pressure:

$$\mathbf{u} \cdot \mathbf{n} = 0; \quad \mathbf{s} \cdot \mathbf{n} = -\left(p_\mathrm{E} + p_\mathrm{G} + p_\mathrm{B}\right); \quad \mathbf{s} \cdot \mathbf{t} = 0\,. \tag{14}$$

For arbitrarily shaped interfaces, as given by Eq. (11), the normal component of the velocity is not necessarily zero. Thus, the interface has to be moved accordingly, while still ensuring its impermeable nature. In the scope of our work, the Arbitrary Lagrangian–Eulerian (ALE) technique was chosen to realize the interface tracking [15, 16]. In simplified terms, the essential idea of ALE for free surface flows is to allow the grid, which is used for discretization, to move independently on the fluid flow. Only the free surface is under constraint, such that the fluid and mesh normal velocity $\mathbf{u} \cdot \mathbf{n} = \mathbf{u}_\mathrm{I} \cdot \mathbf{n}$ equals to the mesh normal velocity $\mathbf{u}_\mathrm{M} \cdot \mathbf{n}$ there. For all other boundaries, $\mathbf{u}_\mathrm{M}$ is restricted differently, according to the modelling. The independent mesh-movement away from the boundaries then allows a free and preferably smooth mesh point distribution. In our case, a Laplace smoothing was utilized (e.g., [17]).

Stationary walls were modelled with the no-slip boundary condition ($\mathbf{u} = 0$), whereas for the moving substrate wall an inhomogeneous Dirichlet boundary condition was necessary ($\mathbf{u} = u_\mathrm{S} \cdot \mathbf{e}_x$, the process x-direction). Along the wetted walls, the interface contact line may have the freedom to slide. Thus, the velocity must not be restricted there directly. To model this behavior, the generalized Navier slip boundary condition was consulted [18, 19]:

$$\mathbf{u} \cdot \mathbf{n} = 0; \quad \mathbf{s} \cdot \mathbf{t} = -\left(\eta/\beta\right) \mathbf{u} \cdot \mathbf{t}\,. \tag{15}$$

The slip length β is present to relate a tangential boundary friction force to the current local slip velocity (it virtually sets $\mathbf{u} = 0$ at a distance β behind the wall). For our calculations, $\beta = 0.01 \cdot h_\mathrm{E}$ was used, where h_E denotes a mean local mesh (element) size of the discretized numerical model.

2. Simulation results. The basis of our analysis was to gain detailed information of all involved fields. To reduce the computational effort, we thought of the melt domain to be fixed during this first step: the magnetic field calculations including the Lorentz force were performed using the finite element solver *OPERA* [20]. The results revealed high amplitudes for $\mathbf{F}_\mathrm{L}$. In Fig. 3 (left), the

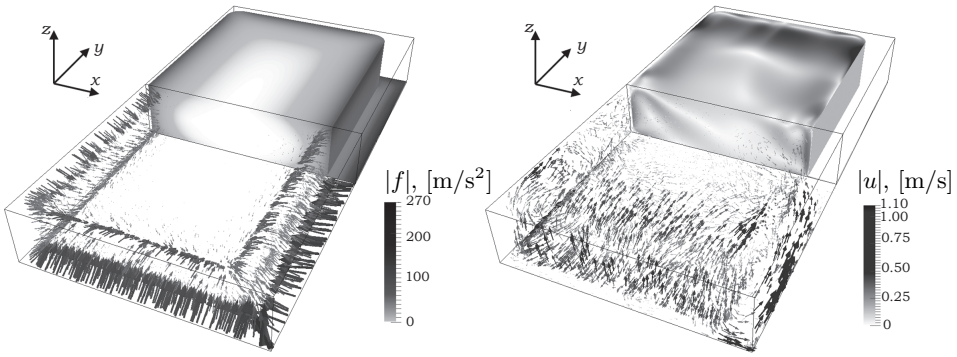

Fig. 3. Lorentz force density (left) and instantaneous velocity field (right) for a fixed fluid domain: in both figures all solid material domains are hidden. The front part shows the related vectors, the rear part the corresponding amplitudes for one half of the fluid domain, respectively. Both parts are separated by the central sectional plane according to Fig. 1. The process direction is indicated by x.

Lorentz force density field $\mathbf{f}_\mathrm{L} = \mathbf{F}_\mathrm{L}/\rho$ reaches values of up to $250\,\mathrm{m/s^2}$ in all regions close to the edges and corners of the fluid domain.

With this in mind, we concluded that the liquid silicon melt would actually be subject to a strong deformation if we had not restricted our model as a premise. The corresponding forced fluid flow for the fixed fluid geometry was simulated with a finite volume solver of the *openFOAM* [21] library suite. We have, therefore, extended the incompressible *pimpleFoam* solver to include an interpolated Lorentz force field from *OPERA*. The computation was conducted on a mesh with $\approx 2.5 \times 10^6$ cells based on the k-ω-SST turbulence model. The resulting velocity field $\mathbf{u}$ is illustrated in Fig. 3 (right) for comparison. The influence of the Lorentz force on the fluid flow is much more intense than the driving force from the moving substrate wall, and that is a substantial finding here. A boundary driving effect of the moving substrate along the x-direction can barely be identified since the global maximum velocity magnitude is more than one order of magnitude higher than the process velocity $\mathbf{u}_\mathrm{S}$.

It is also worth mentioning that our results evidence of two high velocity jets inside the slit region, where the silicon foil is extracted. The jets, of which one is shown in Fig. 3 (right) along the lower right edge, are perpendicular to the process direction and pointing towards the center of the casting frame. This may lead to pressure fluctuations at the trailing meniscus and will be subject to further investigations. Based on our results for the fixed geometry, we assume that the magnetic force is mainly responsible for exciting flow instabilities. As the strong Lorentz force is, however, crucial to balance the gravitational force, it cannot simply be reduced, e. g. shielded, in order to improve the flow behavior for an increased RGS process stability. This can be demonstrated with the help of the magnetic pressure.

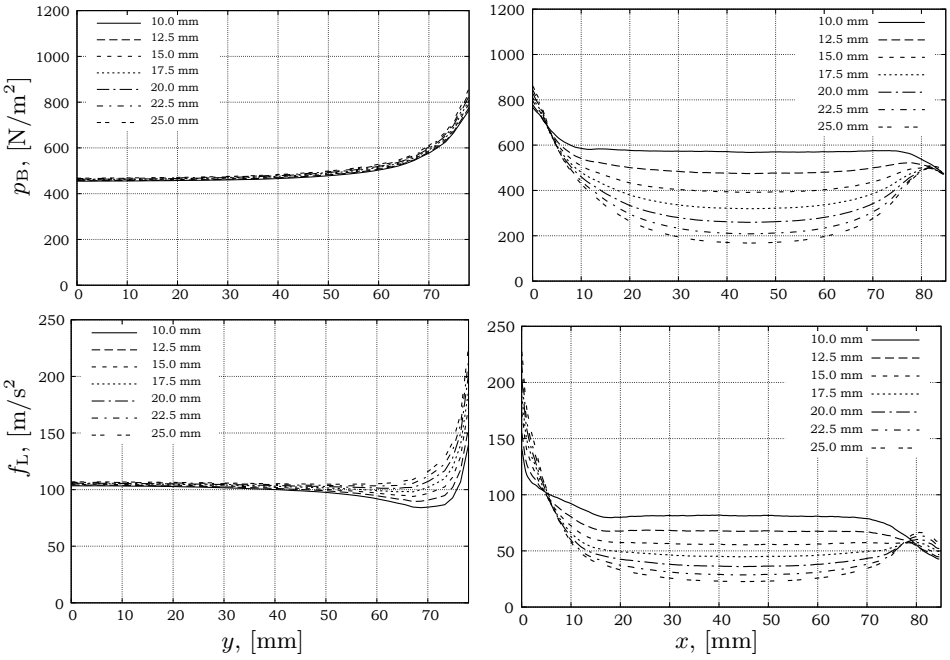

Fig. 4. Magnetic pressure p_B and Lorentz force density $\mathbf{f}_\mathrm{L}$ along the wafer front (left, half width y, center: $y = 0\,\mathrm{mm}$, side: $y = 78\,\mathrm{mm}$) and side (right, arc length $\overline{x}$, front: $\overline{x} = 0\,\mathrm{mm}$, back: $\overline{x} \approx 80\,\mathrm{mm}$) for the varying side wall thicknesses (10–25 mm) of the casting frame.

The top two graphs in Fig. 4 illustrate the magnetic pressure p_B along a wafer side (right) and front (left) for different side wall thicknesses of the casting frame as a result of an investigation on how the melt flow could be shielded to reduce the magnetic forcing on the bulk region. The magnitude of the hydrostatic pressure at the bottom of the casting frame results in $p_\mathrm{G} = \rho g h \approx 506\,\mathrm{N/m^2}$ for a fixed melt level height of $h = 20\,\mathrm{mm}$. On the one hand, comparing p_B with the trends in Fig. 4 (top-right) clearly shows that a properly working magnetic valve, i.e. $p_\mathrm{B} \approx p_\mathrm{G}$, can be numerically proven. On the other hand, the two bottom graphs in Fig. 4 demonstrate the redistribution of the magnetic field due to small geometric changes and the strong dependence between p_B and $\mathbf{f}_\mathrm{L}$, as indirectly given by Eq. (5). In this case, it is even depicted that shielding the wafer only partially may lead to a strong field magnification in some other regions.

Another simulation with the assumption of a fixed melt geometry was performed to find the total system inductivity L of the RGS model depending on the parametrized melt level height h. The power supply of the excitation coil consists of an oscillating circuit operating at a resonance frequency. As the resonance frequency of this circuit changes with L, the idea arose to utilize this behavior for a possible contactless fill level sensing. Fig. 5 shows the total magnetic inductivity $L = W/I_\mathrm{RMS}^2$ of the modelled system against different melt level heights, where W denotes the time-averaged magnetic field energy $W = 1/2 \int \langle \mathbf{H} \cdot \mathbf{B} \rangle_t \mathrm{d}V$. The total system inductivity proved to be not as sensitive as expected for measuring the melt level height based on phase or frequency shifts. There is only a small change of just about 0.3% for L in the range of $h = 5\,\mathrm{mm}$ and $h = 40\,\mathrm{mm}$. Further investigations will show if this is still enough to produce a significant influence on the driving oscillating circuit.

So far, all our presented results were predicated for a fixed melt domain. As we actually get melt deformations due to the high involved Lorentz force density, recent developments were engaged in revising our model to account for the dynamic geometry. To limit the complexity of the extension, we only focused on the top of the fluid domain as a first approach. Modelling the surface movement at the slit regions is expected to be much more demanding in terms of the simulation effort due to its small length scales compared to the whole model.

The Lorentz force acting on a conducting liquid inside a coil roughly points towards the center of this coil. Thus, the shape of the deformed fluid domain for these and similar cases looks similar to a dome. This process is often referred to as

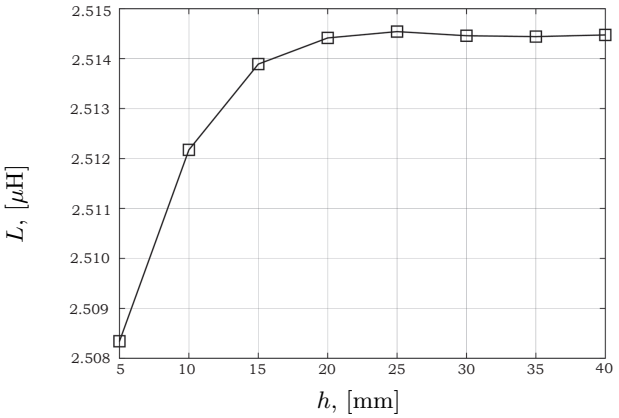

Fig. 5. Magnetic inductivity based on I_RMS for different melt heights h (height along the z-axis).

"dome shaping". Conducting simulations of such (and similar) fully coupled MHD systems with a free surface is part of a broad field of active research to investigate industrial applications, where induction melting or levitation of liquid metals is involved. In recent publications, the work which is closely related to modelling the RGS physics [22–25] is, however, limited to axially symmetric geometries and specialized codes (e.g., SPHINX [22]). Only recently, first three-dimensional simulations have been performed based on a spectral method [26] for liquid droplets and by means of coupling *ANSYS* products [27–31] for more general applications. Coupling solvers or methods (e.g., Spectral, Finite Volume or Finite Element) may generally bring the need of interpolation and thus additional overhead is produced, which means increased computational costs. To circumvent interpolation, we selected a different approach to model the dome shaping for the RGS process. This was realized with *COMSOL Multiphysics* [32], which enabled us to solve all physics (magnetodynamics, fluid dynamics and a moving mesh interface with adaptive re-meshing) within one single Finite Element framework.

The latest results for a 2D simulation of the central longitudinal section of the 3D geometry with a mesh consisting of ≈ 10k elements are presented in Fig. 6. The magnitudes of the Lorentz force (left) and velocity field (right) are in quite good agreement with the central longitudinal section of the 3D model even though the flow pattern has changed. From the shape of the dome and based on the maximum field magnitudes, this demonstrates a manifold f low character and that none of the momentum source terms in Eq. (8) is clearly dominating. This is one major reason, which makes the whole modelling challenging, and simulations require

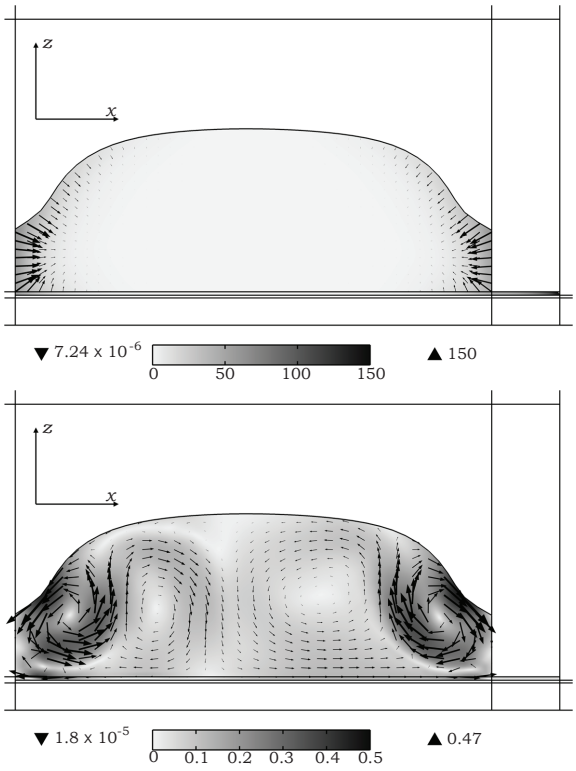

Fig. 6. Dome shaping of the fluid domain for a simplified 2D model (central section of the 3D geometry): time-averaged Lorentz force (top) and fluid velocity (bottom) at the simulation time $t = 3$ s after applying the magnetic field.

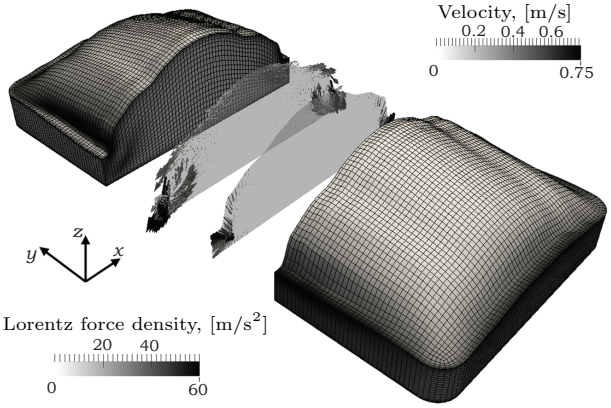

Fig. 7. Dome shaping of the fluid domain for a 3D model (without slit regions): time-averaged Lorentz force (front right part/slice) and fluid velocity (upper left part/slice) at the simulation time $t = 0.2$ s after applying the magnetic field.

high computational costs, especially, in 3D. But it also shows the dominance of the magnetic forcing compared to the driving effect of the moving substrate. Even though the simulation approach with *COMSOL* is promising and very efficient, long-term calculations and deeper flow analysis are still in progress. For several model parameters we experienced stability issues due to geometry parametrization errors with the latest version *4.4* of *COMSOL*. A bug-fix is already scheduled for the upcoming version *5.0* of *COMSOL*.

Owing to the existing problems with *COMSOL 4.4*, we have chosen a different setup for the simulation of the three-dimensional dome shaping. In order to utilize the coupling of two codes with greatly reduced computational overhead due to interpolation, a combination of an adapted *interTrackFoam* [33] solver library of *OpenFOAM Extend Project* and *COMSOL* was used. The Lorentz force calculation with interpolated free surface data was made with *COMSOL*. The resulting data were then iteratively coupled with *interTrackFoam*, which itself was used for flow calculations with interpolated Lorentz force data. As *interTrackFoam* is based on the ALE moving mesh method, it was possible to "carry" the Lorentz force distribution with the mesh for a defined and reasonable small simulation time. This arrangement allowed us to skip the re-calculation of the magnetic fields for a certain amount of time steps to greatly improve the overall performance.

The first results on the basis of this technique are shown in Fig. 7. The maximum Lorentz force density is lower compared to the 2D results because of the omitted slit regions (especially the trailing part). However, the sections through the central bulk region predict similar physics as our 2D-model in terms of the flow pattern, dome shape and field magnitudes. A more comprehensive study is currently being conducted, but it still needs more research and experience. A strong surface tension and a large deformation make high demands to the numerical scheme of the *interTrackFoam* solver and render it sensitive to a set of modelling parameters. Finally, the implementation of the wall contact model has to be improved, too.

3. Conclusion and outlook. The RGS process is a promising technology for future silicon wafer production, but there are some remaining open questions to get it ready for a stable and continuous production. The involved physics are challenging for a numerical investigation which is necessary for improving the pro-

cess controllability and stability. We have successfully performed 3D simulations with a fixed melt geometry to numerically confirm the functioning melt retention based on magnetic fields. It was illustrated that a retention effect is correlated with a forced fluid flow. A parameter study revealed the total system inductivity as a function of the melt level, which might be usable for a fill-level sensing of the silicon melt. Finally, we demonstrate that the surface deformation is substantially important for a satisfactory model. Supported by the results of our work it has become apparent that gaining a detailed insight into the flow and its surface dynamics is a key for controlling the RGS process by means of tailored magnetic fields. Further investigations will address the mentioned stability issues, an improved modelling and general code validation. Additional work will be devoted to reveal how the magnetic field distribution is influenced by different coil geometries, power supply parameters as well as by a different electrical conductivity of the moving substrate.

Acknowledgments. Financial support for this research from the German Helmholtz Association in frame of the Alliance "Liquid Metal Technologies (LIMTECH)" is gratefully acknowledged.

REFERENCES

[1] H. Lange and I. Schwirtlich. Ribbon growth on substrate (RGS) a new approach to high speed growth of silicon ribbons for photovoltaics. *Journal of Crystal Growth*, vol. 104 (1990), no. 1, pp. 108–112.

[2] A. Schönecker, L.J. Geerligs, and A. Müller. Casting technologies for solar silicon wafers: Block casting and ribbon-growth-on substrate. *Solid State Phenomena*, vol. 95-96 (2004), pp. 149–158.

[3] G. Hahn and A. Schönecker. New crystalline silicon ribbon materials for photovoltaics. *Journal of Physics: Condensed Matter*, vol. 16 (2004), no. 50, pp. R1615–R1648.

[4] A. Burgers, *et al.* Near 13% efficiency shunt free solar cells on RGS wafers. In *Photovoltaic Energy Conversion, Conference Record of the 2006 IEEE 4th World Conference on* (2006), vol. 1, pp. 1183–1186.

[5] U. Hess, *et al.* First ribbon growth on substrate (RGS) solar cells with selective emitter. In *26th European Photovoltaic Solar Energy Conference and Exhibition* (2011).

[6] F. Santara, Y. Delannoy, and A. Autruffe. Electromagnetic stirring and retention to improve segregation in silicon for photovoltaics. *Journal of Crystal Growth*, vol. 340 (2012), pp. 41–46.

[7] H.-M. Jeong, H.-S. Chung, and T.-W. Lee. Computational simulations of ribbon-growth on substrate for photovoltaic silicon wafer. *Journal of Crystal Growth*, vol. 312 (2010), no. 4, pp. 555–562.

[8] M. Apel, D. Franke, and I. Steinbach. Simulation of the crystallisation of silicon ribbons on substrate. *Solar Energy Materials and Solar Cells*, vol. 72 (2002), no. 14, pp. 201–208. {EMRS} 2001 Symposium E: Crystalline Silicon for Solar Cells.

[9] K.J. Binns, P.J. Lawrenson, and C.W. Trowbridge. *The Analytical and Numerical Solution of Electric and Magnetic Fields* (Wiley, 1992).

[10] R. Moreau. *Magnetohydrodynamics* (Kluwer, 1990).

[11] T. Morisue. Magnetic vector potential and electric scalar potential in three-dimensional eddy current problem. *IEEE Transactions on Magnetics*, vol. 18 (1982), no. 2, pp. 531–535.

[12] O.C. Zienkiewicz, C. Emson, and P. Bettess. A novel boundary infinite element. *International Journal for Numerical Methods in Engineering*, vol. 19 (1983), p. 393404.

[13] J.H. Ferziger and M. Perič. *Computational Methods for Fluid Dynamics* (Springer, 2002), 3 ed.

[14] R. Scardovell and S. Zaleski. Direct numerical simulation of free surface and interfacial flow. *Annual Review of Fluid Mechanics*, vol. 31 (1999), pp. 567–603.

[15] T.J. Hughes, W.K. Liu, and T.K. Zimmermann. Lagrangian-eulerian finite element formulation for incompressible viscous flows. *Computer Methods in Applied Mechanics and Engineering*, vol. 29 (1981), p. 329349.

[16] J. Donea. Arbitrary lagrangian-eulerian finite element methods. In T. Belytschko and T.R.J. Hughes, editors, *Computational methods for transient analysis* (Elsevier, 1983) p. 473516.

[17] *COMSOL (4.4) Multiphysics Reference Manual*, 2014.

[18] H. Bruus. *Theoretical Microfluidics* (Oxford University Press, 2008).

[19] J.-F. Gerbeau and T. Lelievre. Generalized navier boundary condition and geometric conservation law for surface tension. *Computer Methods In Applied Mechanics and Engineering*, vol. 198 (2009), p. 644656.

[20] Cobham plc. OPERA Simulation Software (http://www.cobham.com), 2014.

[21] OpenCFD Ltd. (ESI Group). OpenFOAM – The open source CFD tool box (http://www.openfoam.com), 2014.

[22] V. Bojarevics and K. Pericleous. Modelling electromagnetically levitated liquid droplet oscillations. *ISIJ INTERNATIONAL*, vol. 43 (2003), no. 6, pp. 890–898.

[23] V. Bojarevics, K. Pericleous, R.A. Harding, and M. Wickins. The development and experimental validation of a numerical model of an induction skull melting furnace. *Metallurgical and Materials Transactions B*, vol. 35 (2004), no. 4, pp. 785–803.

[24] K. Pericleous, *et al.* Experimental and numerical study of the cold crucible melting process. *Applied Mathematical Modelling*, vol. 30 (2006), no. 11, pp. 1262–1280.

[25] V. Bojarevics, A. Roy, and K. Pericleous. Magnetic levitation of large liquid volume. *Magnetohydrodynamics*, vol. 46 (2010), no. 4, pp. 339–352.

[26] S. Easter, V. Bojarevics, and K. Pericleous. Numerical modelling of liquid droplet dynamics in microgravity. *Journal of Physics: Conference Series*, vol. 327 (2011), p. 012027.

[27] S. Spitans, A. Jakovičs, E. Baake, and B. Nacke. Numerical modelling of free surface dynamics of conductive melt in induction crucible furnace. *Magnetohydrodynamics*, vol. 46 (2010), no. 4, pp. 425–436.

[28] S. Spitans, A. Jakovičs, E. Baake, and B. Nacke. Numerical modelling of free surface dynamics of melt in an alternate electromagnetic field. *Magnetohydrodynamics*, vol. 47 (2011), no. 4, pp. 385–397.

[29] S. Spitans, A. Jakovičs, E. Baake, and B. Nacke. Numerical modeling of free surface dynamics of melt in an alternate electromagnetic field: Part i. implementation and verification of model. *Metallurgical and Materials Transactions B*, vol. 44 (2013), no. 3, pp. 593–605.

[30] S. Spitans, E. Baake, A. Jakovičs, and H. Franz. Numerical simulation of electromagnetic levitation in a cold crucible furnace (2014), pp. 256–260.

[31] S. Spitans, E. Baake, and A. Jakovičs. 3d les two-phase flow simulation of convectional electromagnetic levitation melting experiment. In *Proceedings of the 9th PAMIR International Conference* (2014), pp. 261–265.

[32] Comsol Inc. COMSOL Multiphysics (http://www.comsol.com), 2014.

[33] Z. Tukovič and H. Jasak. A moving mesh finite volume interface tracking method for surface tension dominated interfacial fluid flow. *Computers & Fluids*, vol. 55 (2012), no. 0, pp. 70–84.